

Deep learning for seismic phase detection and picking in the aftershock zone of 2008 M_w 7.9 Wenchuan Earthquake

Lijun Zhu^{a,*}, Zhigang Peng^b, James McClellan^a, Chenyu Li^b, DongDong Yao^b,
Zefeng Li^c, Lihua Fang^d

^a*School of Electrical and Computer Engineering
Georgia Institute of Technology
Atlanta, GA 30332, U.S.A.*

^b*School of Earth and Atmospheric Sciences
Georgia Institute of Technology
Atlanta, GA 30332, U.S.A.*

^c*Seismological Laboratory
Division of Geological and Planetary Sciences
California Institute of Technology
Pasadena, CA 91125, U.S.A.*

^d*Institute of Geophysics
China Earthquake Administration
Beijing, 100081, China*

Abstract

The increasing volume of seismic data from long-term continuous monitoring motivates the development of algorithms based on convolutional neural network (CNN) for faster and more reliable phase detection and picking. However, many less studied regions lack a significant amount of labeled events needed for traditional CNN approaches. In this paper, we present a CNN-based Phase-Identification Classifier (CPIC) designed for phase detection and picking on small to medium sized training datasets. When trained on 30,146 labeled phases and applied to one-month of continuous recordings during the aftershock sequences of the 2008 M_W 7.9 Wenchuan Earthquake in Sichuan, China, CPIC detects 97.5% of the manually picked phases in the standard catalog and predicts their arrival times with a five-times improvement over the ObsPy AR picker. In addition, unlike other CNN-based approaches that require millions

*Corresponding author.

Email address: lijun.zhu@gatech.edu (Lijun Zhu)

of training samples, when the off-line training set size of CPIC is reduced to only a few thousand training samples the accuracy stays above 95%. The on-line implementation of CPIC takes less than 12 hours to pick arrivals in 31-day recordings on 14 stations. In addition to the catalog phases manually picked by analysts, CPIC finds more phases for existing events and new events missed in the catalog. Among those additional detections, some are confirmed by a matched filter method while others require further investigation. Finally, when tested on a small dataset from a different region (Oklahoma, US), CPIC achieves 97% accuracy after fine tuning only the fully connected layer of the model. This result suggests that the CPIC developed in this study can be used to identify and pick P/S arrivals in other regions with no or minimum labeled phases.

Keywords: seismic, detection, phase picking, machine learning, CNN

1. Introduction

Event detection and phase picking algorithms are becoming increasingly important for automatic processing of large seismic datasets. Reliable automatic methods for P-wave picking have been available for decades. The commonly adopted approaches for automatic picking of seismic phases convert the time-domain signal to a characteristic function (CF), such as short-term/long-term average (STA/LTA) (Allen, 1982), envelope functions (Baer & Kradolfer, 1987), or autoregressive modeling of Akaike Information Criterion (AR-AIC) (Sleeman & van Eck, 1999), and then select the indices of local maxima, or their rising edges, as the picked arrival times. Higher-order statistics, including kurtosis (Saragiotis et al., 2002) and skewness (Nippres et al., 2010; Ross & Ben-Zion, 2014), have also been used to refine the picks due to their sensitivity to abrupt changes in a time series. These algorithms generally perform better for the P waves than S waves, most likely because S-wave arrivals are usually contaminated by the P coda and converted phases. Polarization has been used to discriminate P and S phases (Jurkevics, 1988). The covariance matrix (Cichowicz, 1993) is used to rotate waveforms into polarized P and S waveform components

using methods such as singular value decomposition (SVD) (Rosenberger, 2010; Kurzon et al., 2014). In general, these existing methods make certain assumptions about the observed seismograms and require careful parameter tweaking when operating on different datasets.

Recently, waveform similarity has been used to detect earthquakes originating from a small region with the same source mechanism while using relatively few parameters (Gibbons & Ringdal, 2006; Shelly et al., 2007; Peng & Zhao, 2009). A subset of the events with high signal-to-noise ratio (SNR) is manually picked as templates to cross-correlate with continuous waveforms to detect smaller events similar to these templates. The computation cost of such template matching methods scales linearly with respect to the number of templates and dataset size. Since the detected events must be similar to one of the template events, this approach is not as general as the aforementioned STA/LTA. Waveform *autocorrelation* is one of the most effective methods to detect nearly repeating seismic signals (Brown et al., 2008). Despite being reliable and robust for different regions, its computation cost scales quadratically with the size of the dataset, making it infeasible when scaled to longer time periods. Further efforts have been devoted to speeding up this process through subspace methods (Harris, 2006; Harris & Dodge, 2011; Barrett & Beroza, 2014), or fingerprint and similarity thresholding (FAST) (Yoon et al., 2015). Recently, inter-station information has also been considered to improve phase picking efficiency and accuracy through inter-station coherence (Delorey et al., 2017), local similarity (Li et al., 2018) and random sampling (Zhu et al., 2017b).

Facilitated by the parallel computation power of modern graphics processing units (GPUs), deep learning (Goodfellow et al., 2016) took off for speech (Hinton et al., 2012) and image recognition (Krizhevsky et al., 2012) applications. Most deep learning studies share the same fundamental network structure, such as the convolutional neural network (CNN), which further reduces the redundant model complexity of a neural network based on local conjunctions of features from the data (often found in images). Unlike waveform similarity methods, CNNs trained on labeled datasets do not need a growing library of templates

and seems to generalize well to waveforms not seen during training. These recent developments have led to CNNs being applied to diverse seismic data sets (Kong et al., 2018), including volcanic events (Luzn et al., 2017), induced seismicity (Perol et al., 2018), aftershocks (Zhu et al., 2018), as well as regular tectonic earthquakes recorded by regional seismic networks (Ross et al., 2018b,a; Zhu & Beroza, 2018). However, most of these works rely on a large volume of labeled training data which is only available in well-studied regions, such as California, US.

In this study, we accommodate the small seismic datasets by designing a specialized CNN network, named CNN-based Phase-Identification Classifier (CPIC), for single-station multi-channel seismic waveforms. The weights of the CNN are obtained via supervised training based on only thousands of human-labeled phase and non-phase samples used in a recent competition for detecting aftershocks of the 2008 M_W 7.9 Wenchuan earthquake in China (Fang et al., 2017). The CNN learns a compact representation of seismograms in the form of a set of nonlinear local filters. From the training process of discriminating seismic events from noise on large datasets, the weights of the local filters collectively capture the intrinsic features that most effectively represent seismograms for the given task of phase picking. In the next sections, we show that CPIC, trained on a much smaller labeled dataset, achieves comparable classification accuracy as reported in Ross et al. (2018a) and Zhu & Beroza (2018). CPIC is further tested on a one-month continuous aftershock dataset for phase detection. It achieves accurate detection of manually picked phases, precise arrival times of picked phases, as well as discovering many weak events not listed in the manual-picking catalog.

2. Data

Unlike recent CNN studies that rely on an exceptionally rich training dataset of labeled samples (Zhu & Beroza, 2018; Ross et al., 2018a) to achieve good accuracy and robustness against noise, we design CPIC and study its performance

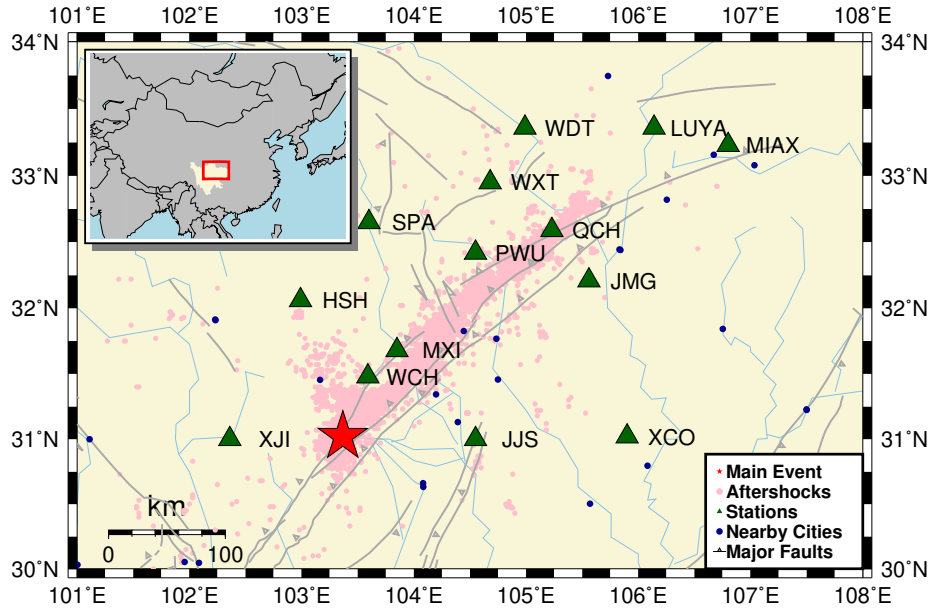
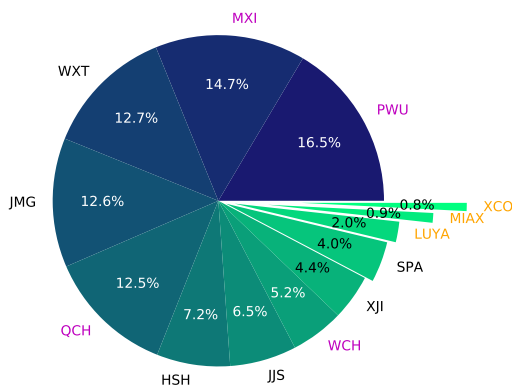


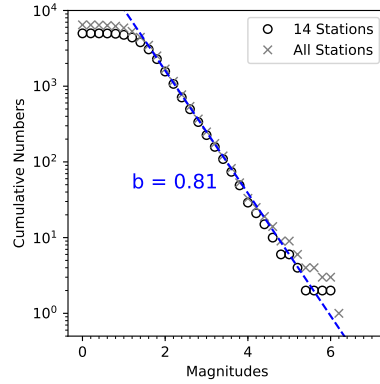
Figure 1: Map showing the study region in Sichuan, China along the aftershock zone of the 2008 M_W 7.9 Wenchuan earthquake (red star). The 9,361 manually picked aftershocks are marked as pink dots. The green triangles mark the 14 permanent stations that were used in this study. The gray and blue thin lines mark active faults and rivers in this region.

on a relatively small training set prior to applying it on a large volume of unlabeled data. This is a typical scenario when analyzing the aftershock dataset of a major earthquake: strong aftershocks at a later time can be easily picked by existing algorithms or analysts; however, the real targets are the numerous number of aftershocks right after the mainshock that are missed by traditional methods (Kagan, 2004; Peng et al., 2006). Prior to CNN training and processing, the only pre-processing applied to the seismogram is soft-clipping via a logistic function which is used to normalize the large dynamic range of the input waveforms. As shown in Appendix B, such pre-processing contributes to CPIC’s stable convergence as well as higher accuracy. Notably, no filtering is applied to the seismic waveforms in pre-processing.

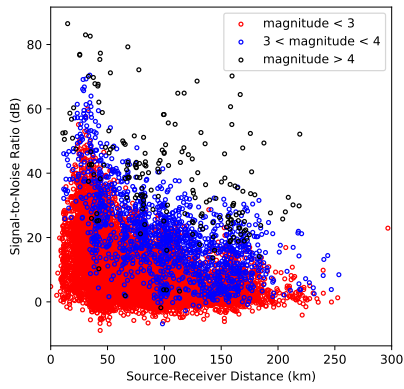
Study region. We utilize the aftershock dataset of the 2008/05/12 M_W 7.9 Wenchuan earthquake that was made available during a recent competition for identify-



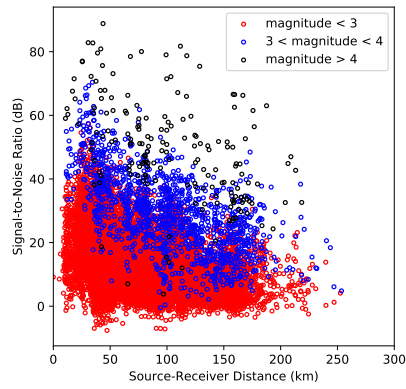
(a) Event distribution over stations



(b) Event distribution over magnitudes



(c) P phases



(d) S phases

Figure 2: Distribution of catalog events in the Wenchuan aftershock dataset for (a) different stations and (b) different magnitudes. Stations on or close to the rupture zone are marked in purple while those far away are marked in gold. Signal-to-noise ratio of picked arrivals against event magnitudes and source-receiver distance for (c) P phases and (d) S phases.

ing seismic phases (Fang et al., 2017). The mainshock occurred on the eastern margin of the Tibetan Plateau (Figure 1), and ruptured the central and northern section of the Longmenshan fault zone (Xu et al., 2009; Feng et al., 2010; Hartzell et al., 2013). Numerous aftershocks occurred following the mainshock, but many of them were still missing in any published earthquake catalogs (Yin

et al., 2018). The aftershock dataset includes continuous data recorded for one month by 14 permanent stations in August 2008, which is three months after the Wenchuan mainshock. Figure 2a shows the distribution of those phases among the 14 stations. Stations near the aftershocks and the rupture zones (e.g., PWU, MXI, WXT, JMG, and QCH) had most of the picked phases, while distant stations (e.g., XCO, MIAX, LUYA, and SPA) have very few; and station WDT has no catalog phase arrivals.

Catalogs. The catalog we used contains 4,986 events with 30,146 phases manually picked on 14 permanent stations with arrivals of P (15,185) of S (14,961) phases. Figure 2b shows the catalog events distributed versus magnitude between ML 0.3 to ML 6.2. The signal-to-noise ratio (SNR) of each phase is computed as the ratio of signal powers between two 4-sec waveforms: one after each phase pick (signal) and one before its corresponding P arrival (noise). Figures 2c and 2d show the distribution of SNR of P and S phases against event magnitudes and source-receiver distance. This catalog was used in a phase picking competition (Zhu et al., 2017a) aiming to improve the detection and picking accuracy from the traditional methods.

Labeled dataset. The CPIC model is trained on a dataset of labeled seismic waveforms in 20-sec long windows. Appendix A provides more details. Adding noise-only windows, which are not included in the original labeled dataset, improves CPIC’s trained performance against noisy seismograms. Here, we assume that quiet regions exist between 60s after an S-wave phase and 60s before a P-wave phase and generate 30,130 noise-only windows. We note that because those noise windows were not verified manually, it is possible that they may include small aftershocks not listed in the catalog. In the end, we obtain a dataset with 60,276 labeled windows, for which P-wave, S-wave, or noise labels have been assigned.

Continuous dataset. Once CPIC is trained on the labeled dataset, the phase detector and arrival picker are then tested on the entire one-month continu-

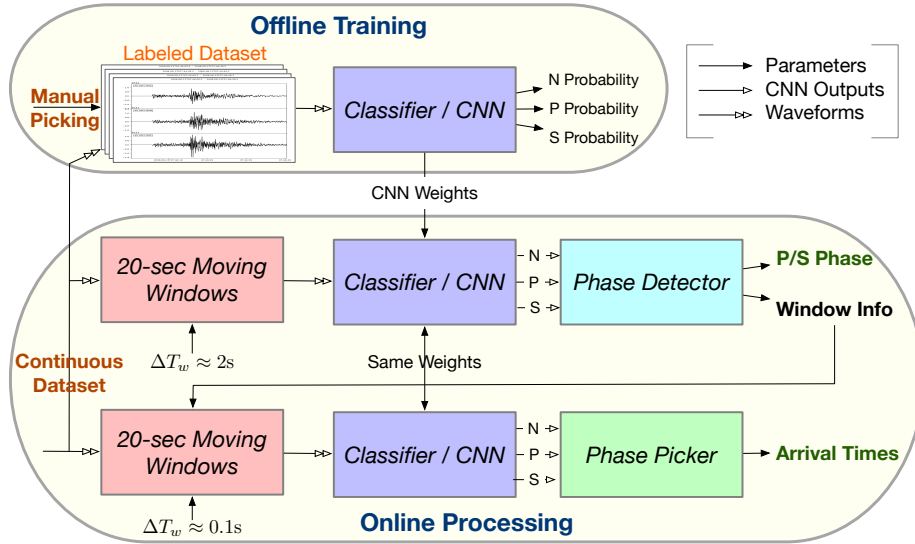


Figure 3: CNN-based Phase-Identification Classifier (CPIC) flow chart. Inputs are three-component seismograms recorded at a single station, labeled in red. Outputs are P-wave, S-wave or noise window probabilities, and picked arrival times for P and S phases, shown in green. The 20-sec moving windows are overlapped with offsets controlled by ΔT_w .

ous waveforms starting on 08/01/2008 00:00:00 Beijing Time (or 07/31/2008 16:00:00 UTC). Due to challenging acquisition conditions in the study area, there are some gaps in the continuous recording. These are filled with zeros to keep the overall dataset consistent while avoiding artificial detections.

3. Method

The task of finding a seismic phase and its arrival time is accomplished in two steps:

1. *Phase detection*: identify time windows where seismic phases exist;
2. *Phase picking*: determine the arrival times of the detected seismic phases within that time window.

In this study, we adopt the processing pipeline summarized in Figure 3. An off-line training process optimizes the parameters of the *CNN-based classifier* iteratively over the labeled dataset. The trained classifier is then used during

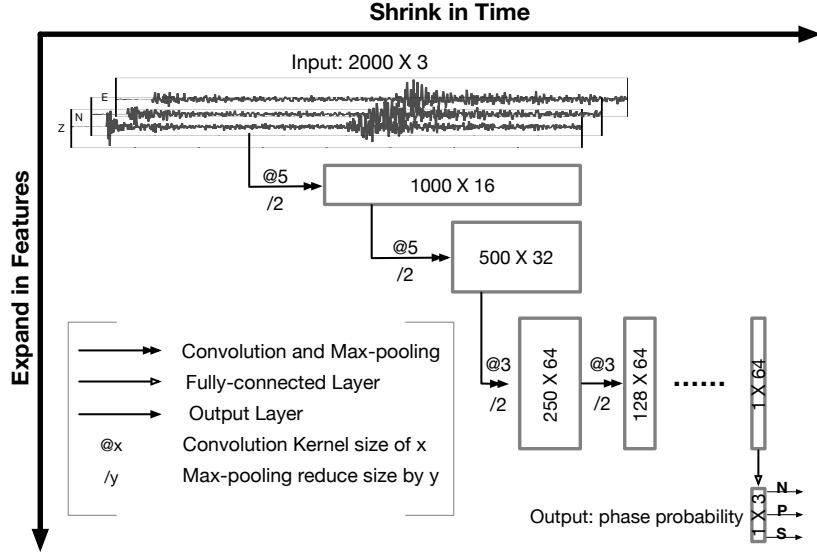


Figure 4: A diagram showing the CNN network structure. Each input is a 3-C seismogram (20-sec window) which shrinks in time but expands in the feature dimension as it passes through 11 convolutional layers for feature extraction. The final layer is fully connected with 3 outputs that give the probabilities of a window being noise, P, and S phases.

on-line processing for both phase detection and picking. The *Phase detector* employs moving windows with 90% overlap ($\Delta T_w = 2$ s offset) and casts seismic phase detection as a classification problem (Zhu et al., 2017c) of P-wave, S-wave, or noise-only labels. The detected windows are then inputted to the same classifier to generate characteristic functions (CFs) on a finely sampled grid, e.g., $\Delta T_w = 0.1$ s offset. The *phase picker* estimates the arrival times based on the peaks of smoothed CFs. Multiple window offsets, ΔT_w , were tested in a grid search manner. In general, a smaller ΔT_w gives better picking accuracy; however, the computation cost is also inversely proportional to ΔT_w .

3.1. CNN-based Classifier

The classifier in Figure 3 operates on inputs that are 3-C seismograms in 20-s windows, sampled at 100 Hz. Its outputs are probabilities of each window containing a P/S phase arrival at 5 s, or only noise. The CNN classifier contains

11 convolutional layers along with one fully-connected layer (Figure 4) It is trained by processing many labeled windows known to contain P or S phases, or noise only.

A *Softmax* function is used to normalize the probabilities in the output layer:

$$q_i(x) = e^{z_i(x)} / (e^{z_0(x)} + e^{z_1(x)} + e^{z_2(x)}) \quad (1)$$

where $i = 0, 1, 2$ represents noise, P, and S classes, and $z_i(x)$ is the unnormalized output of the last fully-connected (FC) layer for the i^{th} class. A loss function is needed when optimizing the CNN weights during the training process, so we use the cross-entropy between a true probability distribution p and the estimated distribution q which is defined as

$$H(p, q) = - \sum_x p(x) \log q(x) \quad (2)$$

Hence, the *Softmax* classifier minimizes the cross-entropy between the estimated class probabilities (q defined in (1)) and the true distribution, which is the distribution where all probability mass is on the correct class, e.g., $p = (0, 1, 0)$ for a labeled P phase window. Between each layer, a rectified linear unit (ReLU) activation function (Nair & Hinton, 2010) introduces nonlinearity into the model. The data size is reduced at each layer using max-pooling (Zhou & Chellappa, 1988).

To accommodate small to medium training set sizes, the proposed CNN uses only one convolution layer between each max-pooling layer. This results in 107,248 parameters in the CNN for a 20-sec window length. The number of parameters can be reduced if a shorter window length is chosen instead. Since each layer down-samples the input data by a factor of two, the model can adjust to a different window length by adding or removing layers. Finally, the number of FC layers used here is fewer than commonly seen in CNNs. We experimented with different numbers of FC layers (one, two, and three) but found no discernible difference in the classifier accuracy. Thus, we chose the structure with fewest FC layers for the sake of simplicity.

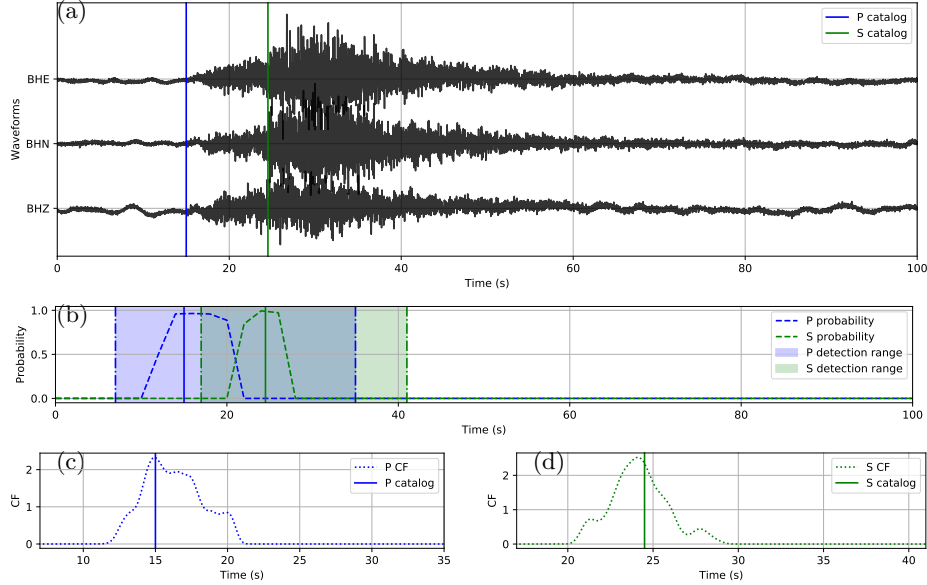


Figure 5: CPIC work flow: (a) Three-component waveforms (catalog P and S arrivals marked) are taken as input; (b) probabilities of both P and S phases are calculated every 2s from which the P and S detection ranges (shaded) are selected, starting 5s before the first nonzero probability sample, and ending 15s after the last. (c, d) Arrival times are picked on characteristic functions (CFs) calculated every 0.1s within each detection range in (b).

3.2. Phase Detector

The phase detector in Figure 3 for continuous processing works on the CNN classifier outputs from moving windows that are coarsely sampled. The three outputs from the CNN classifier are converted to probabilities of noise, P phase, and S phase at each window position by (1). A peak probability above 0.5 is sufficient for detecting a P-phase or S-phase window. Every positive detection provides a candidate 20-sec window that may contain P or S phases. Overlapping windows with the same phase label are merged into one longer window before passing to the phase picker. A detection example of a typical 100-sec waveform is provided in Figure 5b.

The threshold 0.5 for event detection is chosen from the precision-recall tradeoff curve shown in Figure 6 because it gives the highest precision with a

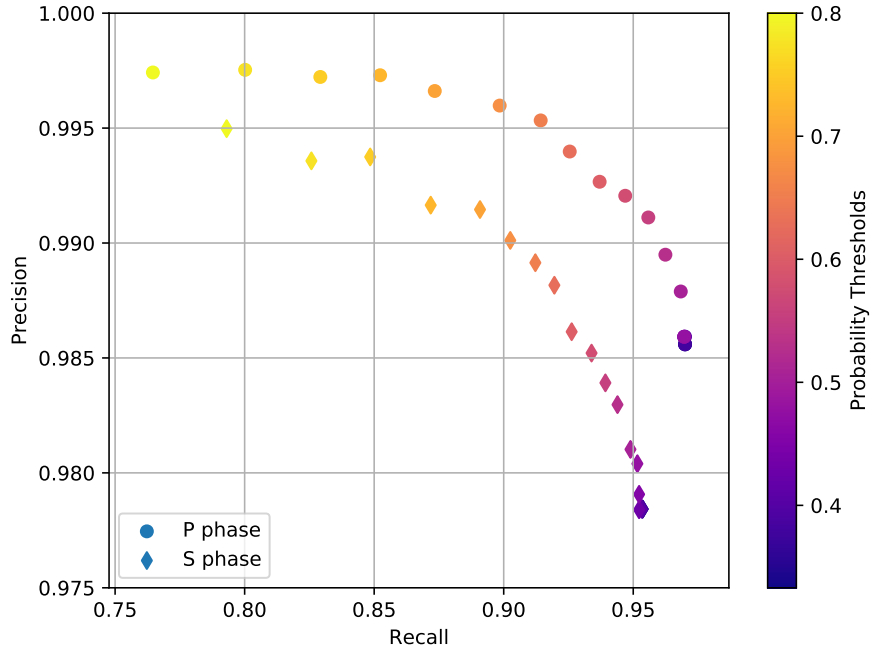


Figure 6: Precision-recall curve for P and S phase detection under different probability thresholds. The top left is the high-precision-low-recall region and the bottom right is the low-precision-high-recall region. A threshold of 0.5 gives the highest precision with recall larger than 0.95. Only P or S phases with a probability higher than both the noise and the threshold are valid detections. This results in the effective minimum threshold at 0.33 for this tri-class classifier.

recall larger than 0.95. Notice that one can remove the constraint that a detected phase needs to have a probability higher than the noise class when weak events are sought in a low-SNR scenario. However, this practice, which increases the false alarm rate and results in a lower precision, is not recommended. This low-precision-high-recall region is not shown in Figure 6), but it would extend the curve further to the right. Note that the confusion matrix shown in Table 1 reflects the best amount of data points for P and S phases in this plot.

3.3. Phase Picker

The phase picker in Figure 3 recomputes the CNN classifier outputs over the detected windows with a smaller offset to obtain the resolution needed for accurate time picking. Since the window of P and S phases starts 5 s prior to the picked arrival time, the probabilities output from the CNN classifier also reflect the likelihood of phase arrivals at 5 s of the given window. Thus, the probability of each phase (the arrival time at 5 s of the corresponding window) should reach a local peak at the true arrival time. Instead of using the probabilities of each phase directly, the *phase picker* relies on characteristic functions (CFs) computed as the smoothed log ratio between probabilities of each phase against the noise class. Using a ratio between phase and noise probabilities makes the constructed CFs adaptive to corresponding noise levels. This helps to eliminate false picks caused by background noise. Picking examples of P and S phases on the detected windows from Figure 5b are given in Figure 5c and 5d, respectively. Comparing to the probabilities in Figure 5b, CFs emphasize the arrival times of P and S phases and suppress the significance of their coda waves.

However, it is possible that multiple picks are present in one single detection window. CPIC does not force a single pick in one window; instead, it assigns a confidence level to each pick. This confidence is measured by the peaks' relative *prominence*, which is defined as the vertical distance between the peak and its lowest contour line (Helman, 2005). This measure makes the picking process parameter-free; however, one can specify a minimum confidence level (e.g., $1/(n+1)$ where n is the number of picks) for a multiple-pick scenario. For example, three picks with confidences level as (0.4, 0.45, 0.15). A 0.25 threshold of confidence rejects the pick with 0.15 prominence while keeping the first two picks. Notice that setting a 0.5 confidence threshold effectively forces a single pick in a detection window.

Table 1: Definition of confusion matrix for evaluating phase detector

		Detector			Total
		Noise	P-wave	S-wave	
Catalog	Noise	N_n	N_p	N_s	$N_n + N_p + N_s$
	P-wave	P_n	P_p	P_s	$P_n + P_p + P_s$
	S-wave	S_n	S_p	S_s	$S_n + S_p + S_s$
Total		$N_n + P_n + S_n$	$N_p + P_p + S_p$	$N_s + P_s + S_s$	ALL

4. Performance Evaluation

CNN Classifier. We can evaluate a CNN classifier by processing labeled testing data where the true output is known. The *accuracy* defined below is a simple measure of a classifier’s performance:

$$\text{accuracy} = \frac{\text{number of correctly labeled samples}}{\text{number of all testing samples}} \quad (3)$$

Noise labels are not treated differently from phase labels, so classifying a noise window correctly has the same weight as confirming a phase window.

Phase Detector. The detector can be viewed as a three-class classifier that decides whether a given time window contains a seismic phase (P or S), or only noise. To evaluate the detector’s effectiveness, we use a confusion matrix as in Table 1, where the labeled windows of each class (per row) are sorted into the number of each detected type (per column). Subscripts denote the detected class, e.g., P_s is the number of windows with P-phase labels but detected as S-phase. The sum of all nine counts equals the total number of labeled windows in the given catalog. To avoid the effect of an imbalanced dataset dominated by noise windows (large N_n), we can use *precision* and *recall* (a.k.a. sensitivity) for each class to measure the performance, which ignores N_n . These are defined for the P-wave class as:

$$\begin{aligned} \text{precision} : \quad \mathcal{P}_p &= \frac{P_p}{N_p + P_p + S_p} \\ \text{recall} : \quad \mathcal{R}_p &= \frac{P_p}{P_n + P_p + P_s} \end{aligned} \quad (4)$$

$\mathcal{P}_n, \mathcal{P}_s, \mathcal{R}_n$ and \mathcal{R}_s can be defined similarly. Notice that both *precision* and *recall* are independent of N_n . Ideally, both \mathcal{P} and \mathcal{R} for each class would be close to 1. However, the labeled aftershock dataset catalog we have is incomplete – it tends to include only the strong and obvious phases while omitting weak events. Thus, higher N_p and N_s counts are expected which lowers \mathcal{P}_p and \mathcal{P}_s , although some of these N_p and N_s detections are likely weak phases not listed in the catalog. On the other hand, \mathcal{R}_p and \mathcal{R}_s should be high if very few manually labeled strong phases are missed. Notice that the accuracy defined in (3) measures the ratio between the sum of diagonal terms over all terms in the confusion matrix:

$$accuracy = \frac{N_n + P_p + S_s}{ALL}$$

Similarly, to avoid a dominant N_n count biasing the accuracy, the F-1 score is computed from *precision* and *recall* (their harmonic mean) for each class:

$$F-1 = \left(\frac{precision^{-1} + recall^{-1}}{2} \right)^{-1} \quad (5)$$

Phase Picker. The phase picking process estimates the arrival time for each detected seismic phase. We measure our phase picker’s error as

$$E_{pick} = T_{pick} - T_{cat} \quad (6)$$

where T_{pick} is the arrival time from CPIC and T_{cat} is the manually picked phase arrival time. Then the systematic bias and variance of our phase picker estimator are measured by taking the mean and standard deviation of E_{pick} over all catalog phases. We expect a close-to-zero bias and reasonably low variance even though the catalog pick itself may contain some human error. Note that the catalog phase arrival time is rounded to the tenth decimal point (0.1).

5. Results

5.1. Training and testing of the CNN classifier

To systematically verify the accuracy and stability of the proposed CNNs, the available 60,000 labeled windows are split into a training subset and a testing subset. The split is done chronologically to emulate a real-world scenario:

Table 2: Confusion matrix for phase classification on the validation dataset which is the latest 20% of the labeled phases.

		Detector			Total
		Noise	P-wave	S-wave	
Catalog	Noise	5,946	97	113	6,156
	P-wave	22	2,930	10	2,962
	S-wave	59	6	2,873	2,938
Total		6,027	3,033	2,996	12,056

Table 3: Precision, recall, and F-1 score for the three classification categories.

Categories	Precision	Recall	F-1 Score
Noise	0.987	0.966	0.976
P-wave	0.966	0.989	0.9787
S-wave	0.959	0.978	0.968

training on historical phases (80%) and testing on future ones (20%). The training process involves minimization of the loss function (2) with iterative updating based on the gradient. After the CNN training process sees every sample in the entire training dataset once, we have finished one *epoch* of training. At the end of each epoch, we generate a testing result to score the CNN classifier accuracy and thus track the progress of its training. Multiple epochs are needed to fully train the CNN weights into a stable state.

Reliable classifier. As demonstrated in Figure 7, the training process of the proposed CNN converges after 40 epochs; no over-fitting is observed even after 200 epochs. The overall validation accuracy of this experiment reaches 97.5%, using the diagonal entries of detailed confusion matrix shown in Table 2. Precision, recall, and F-1 scores are given in Table 3. To further understand characteristics of the trained CNN, we grouped the testing dataset into smaller bins sorted by event magnitude, source-receiver distance, and SNR. The trained CNN is

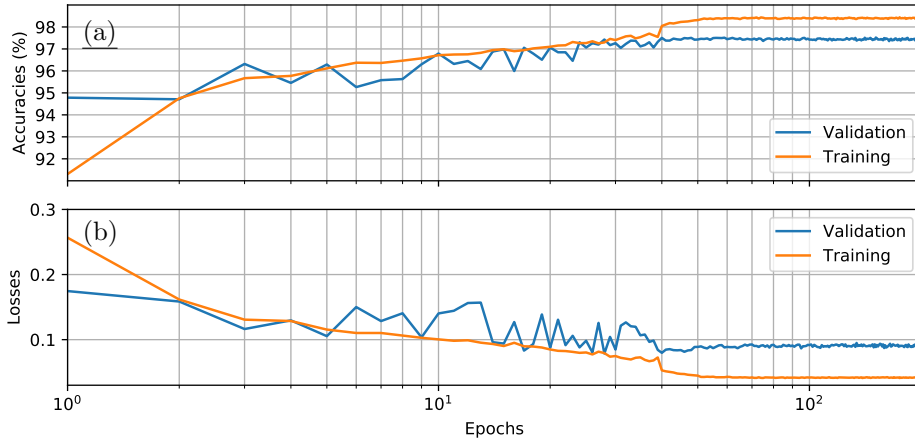


Figure 7: Training performance: (a) classifier accuracy and (b) loss function against number of epochs on training and validation datasets during the CNN training process.

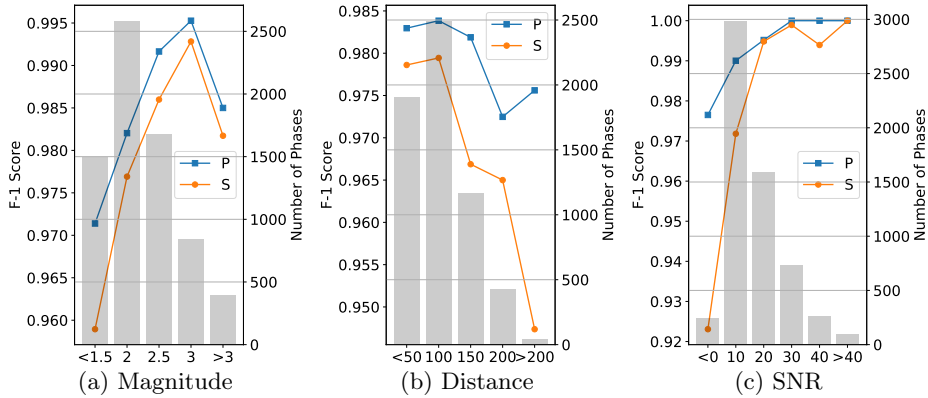


Figure 8: F1 scores (right axes) of the trained classifier versus (a) magnitude, (b) distance, and (c) SNR. P (blue) and S (orange) phases are plotted separately. The number of testing samples in each small bin (left axes) is shown by the bars in the background.

validated on these small testing datasets and its F-1 scores are plotted in Figure 8. The results generally follow our intuition: phases associated with events of larger magnitudes (Figure 8a) and smaller distances (Figure 8b) being classified with higher accuracy. Figure 8c demonstrates that the F-1 score is inversely proportional to the waveform SNR for both P and S phases.

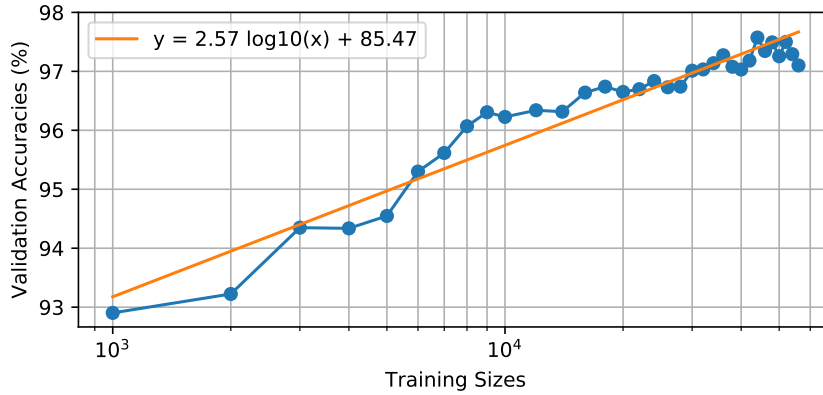


Figure 9: Validation accuracies vs. training dataset sizes (log scale) in blue. A line (log function) is fitted in orange.

Flexible training set size. As mentioned before, the overall 60,276 samples are split into training and validation datasets chronologically with different splitting ratios to explore the minimum required training dataset size. Each split is trained up to 200 epochs and the model accuracy defined in (3) is shown in Figure 9. In general, the relationship between training set size and validation accuracy follows a log function as demonstrated in Figure 9. We note that CPIC reaches 95% accuracy with less than 6,000 training samples and 97% with less than 30,000 training samples. This largely reduces the amount of manual labeling needed to a reasonable level for practical applications. For example, CPIC only requires 300 manually picked aftershock events (for both P and S phases) per station on a 10-station network to achieve 95% classification accuracy.

Fast deployment. CPIC is tested using the Nvidia GTX 1080 Ti GPU with 3,584 CUDA cores and 11 GB memory. The PyTorch machine learning package (Paszke et al., 2017) and ObsPy seismic processing toolbox (Beyreuther et al., 2010) were used to automate our tests. Online processing of one 20-sec window by the trained CNN takes less than 0.3ms on average when feeding the input as 1000 windows per batch to exploit the maximum GPU memory size. This enables us to run the detector on the entire 31-day continuous 3-C waveforms

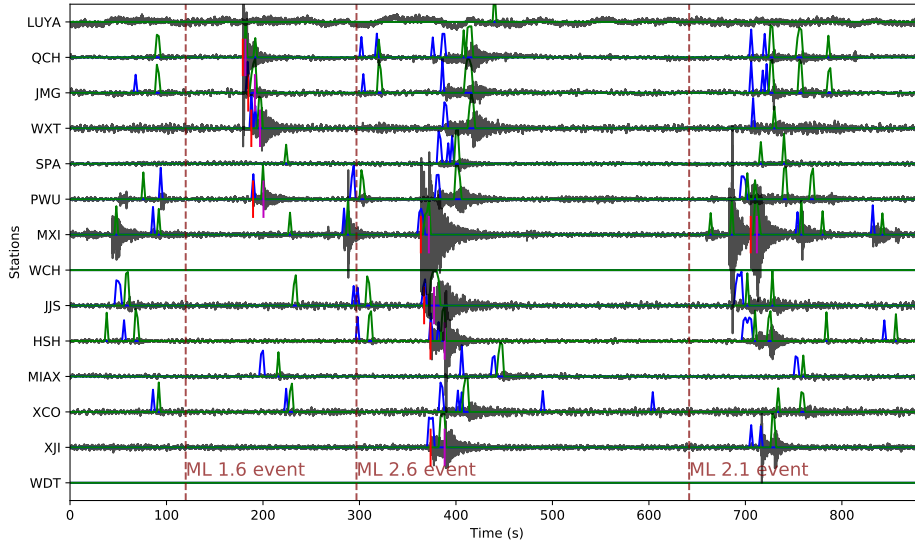


Figure 10: Detection example on 15-minute recording on 14 stations with three catalog events. Only vertical components are plotted. Blue and green curves show the probabilities of P and S phases. Red and magenta bars indicate the catalog P and S arrivals. Origin times of three catalog events are marked by the dashed vertical lines along with their magnitudes.

recorded by 14 stations within two hours. The time spent for phase picking depends on the number of detected phases and the merged window length. In our study, it takes around 12 hours to pick all 30,000 catalog phases within the 31-day dataset.

5.2. Event Detection on Continuous Waveforms

With a 2-sec offset, the continuous waveforms are broken into a collection of 20-sec overlapped time windows for detection (see Figure 3). CPIC gives a label to each such 20-sec window as P phase, S phase, or noise. Consecutive windows with the same label are merged into one longer window (Figure 5b), e.g., four neighboring 20-sec windows expand to a 28-sec window. As shown in Table 3, 98.6% and 97.8% of the catalog P and S phases are correctly detected (recall), while 97.0% and 95.4% detected P and S phases match a catalog phase (precision).

Figure 10 shows the application of the CPIC detector on a 15-minute con-

Table 4: Evaluation metrics for CPIC and ObsPy AR picker on the validation dataset.

Method	$\mu(E_p)$	$\mu(E_s)$	$\sigma(E_p)$	$\sigma(E_s)$
CPIC picker (ms)	-79.0	-78.9	138.8	293.0
ObsPy AR picker (ms)	311.4	936.3	671.6	1,697.0

tinuous section across all 14 stations. For the three catalog events (ML 1.6, 2.6, and 2.1, respectively), the CPIC detector finds all phases picked in the catalog (marked by vertical bars in red for P phase and magenta for S phase). Moreover, it detects additional phases for these three events on other stations that were missed by manual picking, e.g., P (blue peak) and S (green peak) phases around 400s on five additional stations (SPA, QCH, PWU, MIAX, and WXT) for the ML 2.6 event.

On the other hand, additional phases are also detected, which might be associated with events missed in the catalog. For example, two clusters of phases around 80s and 300s in Figure 10 exhibit reasonable moveout curves and may correspond to legitimate events. To investigate these additional phase detections, we built a matched-filter (MF) enhanced catalog for one day (8/30/2008) following the procedure used by Meng et al. (2013) (details explained in Appendix C). This MF catalog expands the original 150 events and 968 phases into 1,300 events and 12,200 phases for that day. During the same time, CPIC detects 4,123 seismic phases among which 2,892 (70%) contain a phase in the MF catalog. Further studies are needed to check whether the remaining 30% correspond to actual events that are not similar to existing templates.

5.3. Phase Picking on Catalog Events

Picking Results. The detected windows are reprocessed by the CNN with a 0.1 s offset to generate the CPIC arrival times. The picked arrival times are compared with the catalog phase arrivals and results from the ObsPy AR picker. The error defined in (6) is used to measure the performance of the P and S phase pickers separately. Table 4 summarizes the statistics of picking errors for P and S phases

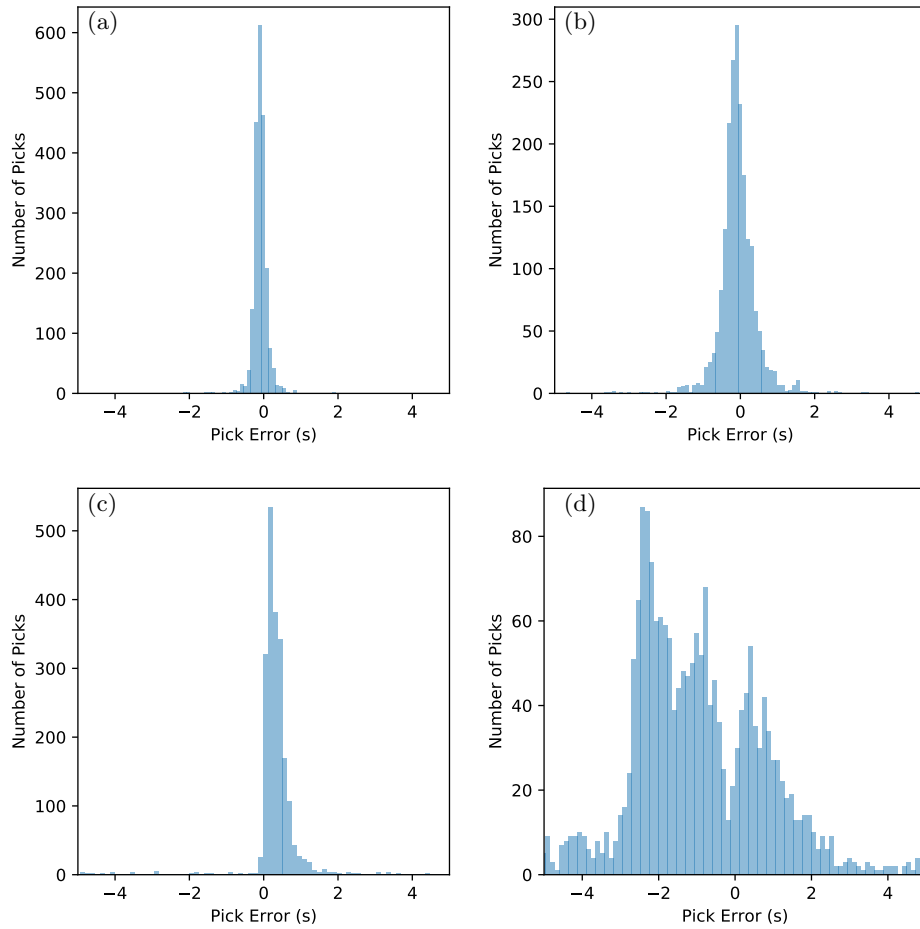


Figure 11: The distributions of picking errors (E_{pick}) of CPIC (upper panels) and ObsPy AR picker (lower panels) on the validation dataset.

from CPIC and the ObsPy AR picker. Errors for both P and S phases from CPIC have much smaller standard deviations and biases than their counterparts from the ObsPy AR picker. Significant improvements are observed by applying CPIC, especially for S-wave arrival times. This is expected since picking S phase arrivals is more challenging for traditional methods due to interference from the P wave coda. Figure 11 compares the distributions of picking errors for P and S phases from CPIC with the ObsPy AR picker. The error distributions from both methods for P arrivals are narrower than those for S waves. This is consistent

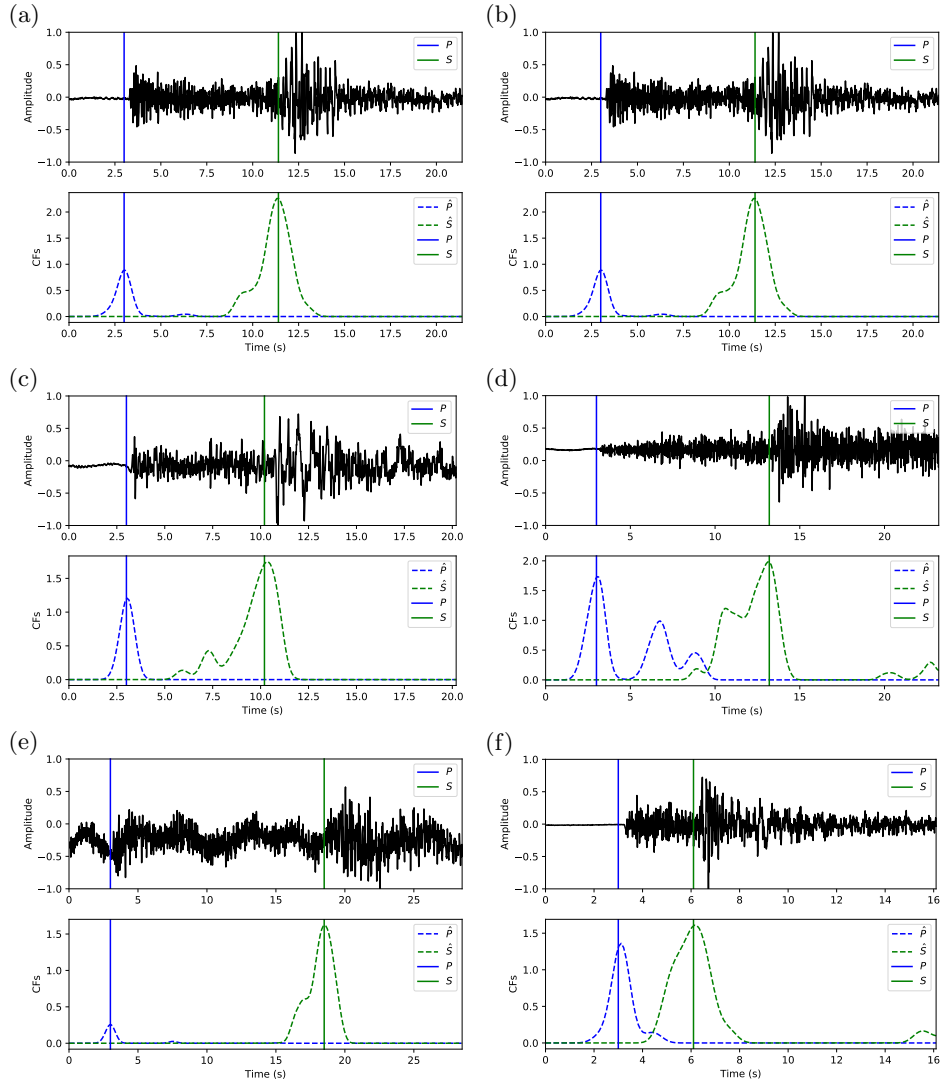


Figure 12: Examples of CPIC picks that are consistent with manual picks. The upper panels of (a)–(f) are the vertical components from the 3-C waveforms used in the picking process. Vertical lines denote arrival-time picks. The lower panels show the characteristic functions (CFs) of \hat{P} (blue) and \hat{S} (green) used by CPIC to pick the arrival times.

with our intuition that P phase arrivals are clear and easier to pick. Notice that both distributions from CPIC are more symmetric than those from ObsPy AR picker.

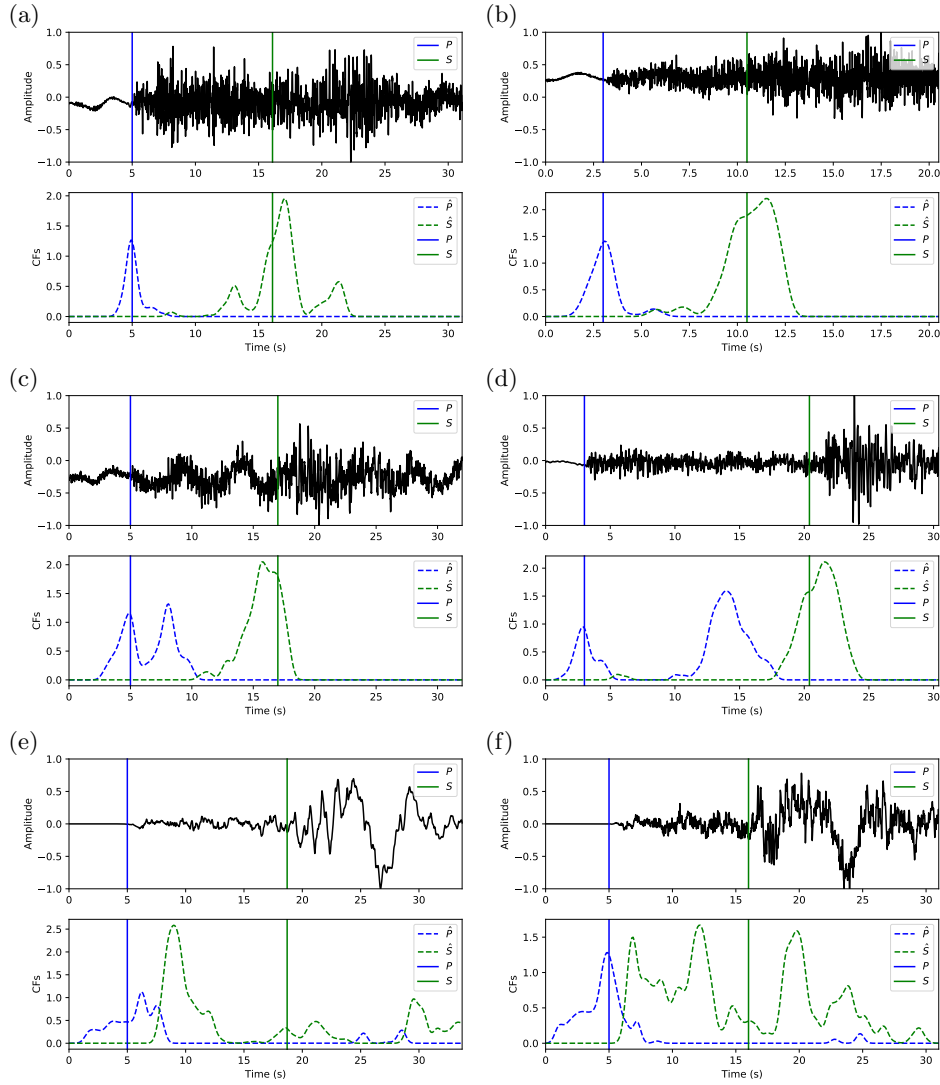


Figure 13: Examples of CPIC picks that are inconsistent with manual picks. (a, b) are examples of ambiguous S picks. (c, d) are examples of multiple P picks. (e, f) are examples of an ML 6.1 events on two distant stations.

Picking Examples. Examples of arrival picking are given in Figure 12 and 13 to demonstrate CPIC’s performance. Note that the waveforms displayed in the upper panels have mean removed and are scaled to have a maximum amplitude of one; however, the real inputs to the CPIC model are the original raw

waveforms. Figures 12a and 12b show the ideal cases where there is only one distinct peak in the CFs of both P and S phases that aligns perfectly with the catalog arrival times. Multiple peaks are present in Figure 12c and 12d, but the CPIC picks correctly matched the manual picks. Less ideal cases are shown in Figure 12e and 12f where CPIC picks the correct arrival times but may have issues when the conditions are worse. The noisy waveform in Figure 12e results in a small peak for P wave around 3 s, which may be buried under the noise floor if more severe noise were present. CPIC picked the arrival times in Figure 12f correctly but has a small tail for the S phase at the end. This small tail was successfully rejected due to its small amplitude, but it may become a false alarm if the relative peak amplitude of the S phase around 6 s were much smaller. This is also the case for Figure 12d. Examples of picks inconsistent with the catalog arrival times are also shown in Figure 13. Unlike multiple peak cases shown in Figure 12, the peak CFs from CPIC in Figure 13c and 13d is more than 1 s from the manually picked arrivals. Figure 13e and 13f show incorrect picks of a M_W 6.1 event on two distant stations (SPA and WXT). Since there are only two events with magnitude larger than M_W 6 in the given Wenchuan catalog, the trained model is “inexperienced” with such large events. This is one of the disadvantages for training-based approaches: the model needs to see enough examples before it can provide reliable predictions.

6. Discussion

In this study, we designed CPIC to classify a 20-sec time window as noise, P phase or S phase based on training a CNN over a set containing 60,000 manually labeled windows. The resulting classifier not only achieves more than 97% accuracy for its original classification task but also serves as a key component for phase detection and picking. The training process tweaks the weights of filters in the CNN model and reinforces the knowledge of seismic phase characteristics by iterative updates. The resulting knowledge, encapsulated in the CNN representation of the continuous data, helps us to easily design a straightforward

detection and picking system for seismic phases. By using overlapping 20-sec windows with a fixed offset, the trained CNN provides a continuous output of probability values for its noise, P-phase, and S-phase classes.

6.1. Comparison with other CNN approaches

Another way to exploit deep learning for phase picking is to train the CNN for detection outputs and phase picking outputs directly. As demonstrated in Zhu & Beroza (2018), a likelihood function of seismic phases can be estimated for a given waveform instead of individual classification on each data point. Trained on over a million labeled waveforms in Northern California (NCEDC 2014), PhaseNet (Zhu & Beroza, 2018) achieves better picking accuracy (51.5 vs. 138.8 ms for P and 82.9 vs. 293.0 ms for S). However, we note that our dataset has not only more than one order-of-magnitude fewer labeled samples, but also challenging picking conditions—the benchmarks from the ObsPy AR picker have ten-times-larger standard deviation of picking errors. As shown in Figure 11c and 11d, the STA/LTA based AR-AIC picking method results in large uncertainty of the picked arrival times. This is drastically different from the condition in Zhu & Beroza (2018) where the AR-AIC method results in picking errors with less than 200 ms standard deviation. Since our catalog is limited in the number of labeled waveforms and more challenging conditions, we elected to keep the picker simple and focus on the effectiveness of the CNN for feature extraction.

When comparing with Ross et al. (2018a), the proposed CNN yields comparable detection accuracy (97.4% vs. > 99%) even though it uses a relatively small training dataset (40,000 vs. > 1 million training samples). This is mainly because the task that the CNN classifiers are trained on is rather simple—the CNN easily extracts the key features that are needed to effectively separate the noise, P, and S phase windows from each other. This agrees with our intuition and the role of human analysts: noise, P phase, and S phase are very distinctive in good SNR cases. Just as analysts learn to pick correct seismic phases by looking at examples of P and S phases, our CNN classifiers are trained on good

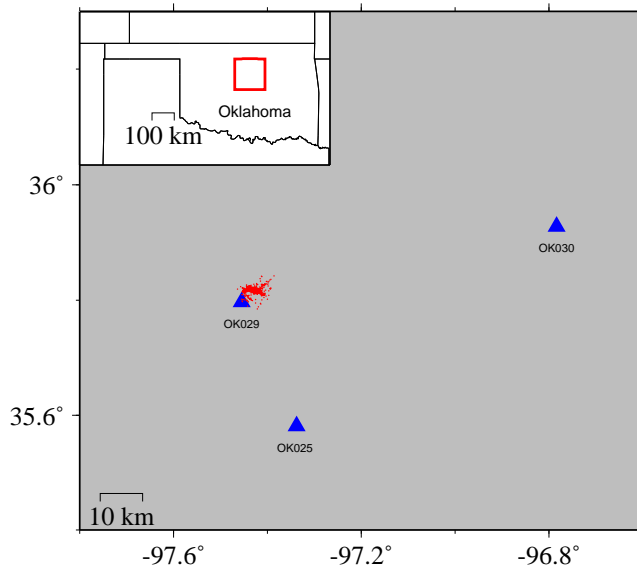


Figure 14: Map of study region in Oklahoma, central U.S. Red dots are 890 events with P and S phase arrivals and blue triangles are broadband stations of the US Geological Survey Network (GS).

SNR cases labeled by manual picking. Compared to traditional methods, the CNN can be applied quickly and automatically to a large volume of data with more challenging conditions, such as variable SNR.

6.2. CPIC applied to induced earthquake dataset in Oklahoma, USA

To validate how well CPIC generalizes to another dataset, we apply the CNN trained on aftershocks in Wenchuan, China to a dataset containing likely human-induced earthquakes in Oklahoma (OK), USA (Chen et al., 2018). As shown in Figure 14, 890 events were manually picked with P and S phases on three stations (OK025, OK029, and OK030). This results in a small catalog dataset with approximately 5,000 labeled samples. When we applied the original CPIC classifier trained on the Wenchuan dataset, it achieved accuracy above 90% on the two near stations (OK025 and OK029), but not on the far station (OK030) as shown in Table 5.

Next, we retrained the model by fine-tuning only the fully-connected (FC)

Table 5: CPIC accuracy when testing on a three-station seismic dataset in OK, USA. The first row shows the performance of directly applying CPIC as trained on the Wenchuan, China dataset, while the second row shows the enhanced accuracy after fine-tuning CPIC on 2,000 training samples from the Oklahoma region.

Station	OK025	OK029	OK030	All
Original (%)	95.7	92.2	69.9	87.5
Fine-tuned (%)	98.8	96.2	94.2	97.0

layer that classifies feature vectors into probabilities of phase/noise classes; the 11 convolutional layers were kept fixed. After fine-tuning the classifier on approximately 2,000 samples (≈ 350 events), the accuracy on all three stations is above 94% with an overall accuracy at 97.0%. This shows that the convolutional layers in the CPIC model capture the essential representation of a seismic wave needed for phase classification. After fine-tuning the classification layer (FC), the CPIC model trained on one region can be generalized to other regions for different event types (aftershocks vs. induced earthquakes).

7. Conclusions

In this and other recent studies, CNNs have shown clear potential for efficiently processing large volumes of seismic waveform data with accurate results. Usually, CNN-based approaches require a large training dataset with accurate labels, provided by human analysts. In this paper, we demonstrated an alternative path when using deep learning for seismic processing. Instead of designing and training a CNN to accomplish the phase detection and picking tasks directly, we trained a CNN-based classifier that categorizes a seismic window into three classes: P, S, or Noise. This allows us to train a relatively simple CNN with a smaller training set. The detection and picking task is then accomplished by repeatedly applying the classifier on overlapping windows from continuous waveforms.

We named this processing framework CPIC and tested it on 3-C data collected from the aftershock zone of the 2008 M_W 7.9 Wenchuan earthquake. CPIC achieves over 97.5% phase detection rate while finding a significant number of potential phases missed by manual picking. CPIC also has a phase picking accuracy for which almost all of its picks are within ± 300 ms of the manually labeled picks (Figure 11). More importantly, CPIC’s processing time is remarkably small: on a desktop workstation with an Nvidia GTX1080 Ti GPU, it takes 2 hrs to detect and 12 hrs to pick phases on 3-C continuous data recorded for 31 days on 14 stations. When compared to an expanded catalog for one day, the aggregation of picks by CPIC on all stations detects all events found by manual picking and finds additional events missed by manual picking. Furthermore, 70 % of the picks from CPIC can be confirmed by a matched filter enhanced catalog. The trained model also reached 97% accuracy on a dataset from a different region after fine-tuning one layer of the model on a small training set. Thus CPIC has the potential to be applied to regions where manual pickings are sparse, but a large volume of unpicked waveforms is available.

References

- Allen, R. (1982). Automatic phase pickers: Their present use and future prospects. *Bulletin of the Seismological Society of America*, *72*, S225.
- Baer, M., & Kradolfer, U. (1987). An automatic phase picker for local and teleseismic events. *Bulletin of the Seismological Society of America*, *77*, 1437.
- Barrett, S. A., & Beroza, G. C. (2014). An empirical approach to subspace detection. *Seismological Research Letters*, *85*, 594.
- Beyreuther, M., Barsch, R., Krischer, L., Megies, T., Behr, Y., & Wassermann, J. (2010). ObsPy: a python toolbox for seismology. *Seismological Research Letters*, *81*, 530–533.
- Brown, J. R., Beroza, G. C., & Shelly, D. R. (2008). An autocorrelation method to detect low frequency earthquakes within tremor. *Geophysical Research Letters*, *35*.
- Chen, X., Haffener, J., Goebel, T. H. W., Meng, X., Peng, Z., & Chang, J. C. (2018). Temporal correlation between seismic moment and injection volume for an induced earthquake sequence in central oklahoma. *Journal of Geophysical Research: Solid Earth*, *123*, 3047–3064.
- Cichowicz, A. (1993). An automatic S-phase picker. *Bulletin of the Seismological Society of America*, *83*, 180–189.
- Delorey, A. A., van der Elst, N. J., & Johnson, P. A. (2017). Tidal triggering of earthquakes suggests poroelastic behavior on the San Andreas fault. *Earth and Planetary Science Letters*, *460*, 164 – 170.
- Fang, L., Wu, Z., & Song, K. (2017). SeismOlympics. *Seismological Research Letters*, *88*, 1429.
- Feng, G., Hetland, E. A., Ding, X., Li, Z., & Zhang, L. (2010). Coseismic fault slip of the 2008 Mw 7.9 Wenchuan earthquake estimated from InSAR and GPS measurements. *Geophysical Research Letters*, *37*.

- Gibbons, S. J., & Ringdal, F. (2006). The detection of low magnitude seismic events using array-based waveform correlation. *Geophysical Journal International*, *165*, 149–166.
- Goodfellow, I., Bengio, Y., & Courville, A. (2016). *Deep Learning*. MIT Press.
- Harris, D. B. (2006). *Subspace detectors: theory*. Technical Report Lawrence Livermore National Laboratory (LLNL), Livermore, CA.
- Harris, D. B., & Dodge, D. A. (2011). An autonomous system for grouping events in a developing aftershock sequence. *Bulletin of the Seismological Society of America*, *101*, 763.
- Hartzell, S., Mendoza, C., RamirezGuzman, L., Zeng, Y., & Mooney, W. (2013). Rupture history of the 2008 Mw7.9 Wenchuan, China, earthquake: Evaluation of separate and joint inversions of geodetic, teleseismic, and strongmotion data. *Bulletin of the Seismological Society of America*, *103*, 353.
- Helman, A. (2005). *The Finest Peaks-Prominence and Other Mountain Measures*. Trafford Publishing.
- Hinton, G., Deng, L., Yu, D., Dahl, G. E., r. Mohamed, A., Jaitly, N., Senior, A., Vanhoucke, V., Nguyen, P., Sainath, T. N., & Kingsbury, B. (2012). Deep neural networks for acoustic modeling in speech recognition: The shared views of four research groups. *IEEE Signal Processing Magazine*, *29*, 82–97.
- Jurkevics, A. (1988). Polarization analysis of three-component array data. *Bulletin of the Seismological Society of America*, *78*, 1725.
- Kagan, Y. Y. (2004). Short-term properties of earthquake catalogs and models of earthquake source. *Bulletin of the Seismological Society of America*, *94*, 1207–1228.
- Kong, Q., Trugman, D. T., Ross, Z. E., Bianco, M. J., Meade, B. J., & Gerstoft, P. (2018). Machine learning in seismology: Turning data into insights. *Seismological Research Letters*, *90*, 3.

- Krizhevsky, A., Sutskever, I., & Hinton, G. E. (2012). Imagenet classification with deep convolutional neural networks. In F. Pereira, C. J. C. Burges, L. Bottou, & K. Q. Weinberger (Eds.), *Advances in Neural Information Processing Systems 25* (pp. 1097–1105). Curran Associates, Inc.
- Kurzton, I., Vernon, F., Rosenberger, A., & Ben-Zion, Y. (2014). Real-time automatic detectors of P and S waves using singular value decomposition. *Bulletin of the Seismological Society of America*, *104*, 1696–1708.
- Li, Z., Peng, Z., Hollis, D., Zhu, L., & McClellan, J. (2018). High-resolution seismic event detection using local similarity for Large-N arrays. *Scientific Reports*, *8*, 1646.
- Luzn, M. T., Rodriguez, A. B., Martinez, L. G., Benitez, C., & Ibez, J. M. (2017). Automatic classification of volcano-seismic events based on deep neural networks. In *Abstract presented at 2017 Fall Meeting, AGU S41D-01*. New Orleans, LA.
- Meng, X., Peng, Z., & Hardebeck, J. L. (2013). Seismicity around Parkfield correlates with static shear stress changes following the 2003 Mw 6.5 San Simeon earthquake. *Journal of Geophysical Research: Solid Earth*, *118*, 3576–3591.
- Nair, V., & Hinton, G. E. (2010). Rectified linear units improve restricted boltzmann machines. In *Proceedings of the 27th international conference on machine learning (ICML-10)* (pp. 807–814).
- Nippres, S. E. J., Rietbrock, A., & Heath, A. E. (2010). Optimized automatic pickers: application to the ANCORP data set. *Geophysical Journal International*, *181*, 911–925.
- Paszke, A., Gross, S., Chintala, S., Chanan, G., Yang, E., DeVito, Z., Lin, Z., Desmaison, A., Antiga, L., & Lerer, A. (2017). Automatic differentiation in PyTorch. In *Advances in Neural Information Processing Systems 30*.

- Peng, Z., Vidale, J. E., & Houston, H. (2006). Anomalous early aftershock decay rate of the 2004 Mw 6.0 Parkfield, California, earthquake. *Geophysical Research Letters*, *33*.
- Peng, Z., & Zhao, P. (2009). Migration of early aftershocks following the 2004 Parkfield earthquake. *Nature Geoscience*, *2*, 877.
- Perol, T., Gharbi, M., & Denolle, M. (2018). Convolutional neural network for earthquake detection and location. *Science Advances*, *4*.
- Rosenberger, A. (2010). Real-time ground-motion analysis: distinguishing P and S arrivals in a noisy environment. *Bulletin of the Seismological Society of America*, *100*, 1252–1262.
- Ross, Z., & Ben-Zion, Y. (2014). An earthquake detection algorithm with pseudo-probabilities of multiple indicators. *Geophysical Journal International*, *197*, 458–463.
- Ross, Z. E., Meier, M., Hauksson, E., & Heaton, T. H. (2018a). Generalized seismic phase detection with deep learning (short note). *Bulletin of the Seismological Society of America*, *108*, 2894.
- Ross, Z. E., Meier, M.-A., & Hauksson, E. (2018b). P-wave arrival picking and first-motion polarity determination with deep learning. *Journal of Geophysical Research: Solid Earth*, .
- Saragiotis, C. D., Hadjileontiadis, L. J., & Panas, S. M. (2002). PAI-S/K: a robust automatic seismic P phase arrival identification scheme. *IEEE Transactions on Geoscience and Remote Sensing*, *40*, 1395–1404.
- Shelly, D. R., Beroza, G. C., & Ide, S. (2007). Non-volcanic tremor and low-frequency earthquake swarms. *Nature*, *446*, 305307.
- Sleeman, R., & van Eck, T. (1999). Robust automatic P-phase picking: An on-line implementation in the analysis of broadband seismogram recordings. *Physics of the earth and planetary interiors*, *113*, 265–275.

- Xu, X., Wen, X., Yu, G., Chen, G., Klinger, Y., Hubbard, J., & Shaw, J. (2009). Coseismic reverse- and oblique-slip surface faulting generated by the 2008 Mw 7.9 Wenchuan earthquake, China. *Geology*, *37*, 515.
- Yin, X., Chen, J.-h., Peng, Z., Meng, X., Liu, Q., Guo, B., & Cheng Li, S. (2018). Evolution and distribution of the early aftershocks following the 2008 Mw 7.9 Wenchuan earthquake in Sichuan, China. *Journal of Geophysical Research: Solid Earth*, .
- Yoon, C. E., O'Reilly, O., Bergen, K. J., & Beroza, G. C. (2015). Earthquake detection through computationally efficient similarity search. *Science Advances*, *1*.
- Zhou, Y. T., & Chellappa, R. (1988). Computation of optical flow using a neural network. In *IEEE 1988 International Conference on Neural Networks* (pp. 71–78 vol.2).
- Zhu, L., Li, Z., Li, C., Wang, B., Chen, Z., McClellan, J. H., & Peng, Z. (2017a). Machine-learning inspired seismic phase detection for aftershocks of the 2008 MW 7.9 Wenchuan earthquake. In *Abstract presented at 2017 Fall Meeting, AGU S41D-08*. New Orleans, LA.
- Zhu, L., Liu, E., McClellan, J., Zhao, Y., Li, W., Li, Z., & Peng, Z. (2017b). Estimation of passive microseismic event location using random sampling-based curve fitting. In *SEG Technical Program Expanded Abstracts 2017* (pp. 2791–2796).
- Zhu, L., Liu, E., McClellan, J. H., Peng, Z., & Li, Z. (2017c). Classification of arrival-time picks for microseismic event localization. In *79th EAGE Conference and Exhibition 2017*.
- Zhu, L., Peng, Z., & McClellan, J. (2018). Deep learning for seismic event detection of earthquake aftershocks. In *52nd Annual Asilomar Conference on Signals, Systems, and Computers*. Pacific Grove, CA.

Zhu, W., & Beroza, G. C. (2018). PhaseNet: a deep-neural-network-based seismic arrival time picking method. *arXiv preprint arXiv:1803.03211*, .

Appendix A. Window length

For each manually picked phase, we define a 20-sec long window starting 5s before the pick and ending 15s after as one window of a seismic phase (Figure A.1). A long time window was chosen so that there is a high likelihood that a P-wave window contains some S-wave at its end and that S-wave windows contain some P-wave coda at the beginning. This window definition implicitly embeds the normal sequential relationship between P and S wave phases in the labeled dataset itself. As shown in Table A.1, some other typical windows lengths were tested, and those larger than 10s worked better for this dataset.

Table A.1: Classifier accuracy (defined in (3)) vs. window lengths.

Window Length (sec)	2.5	5	10	20	40
Accuracy(%)	94.7	96.3	96.9	97.4	97.2

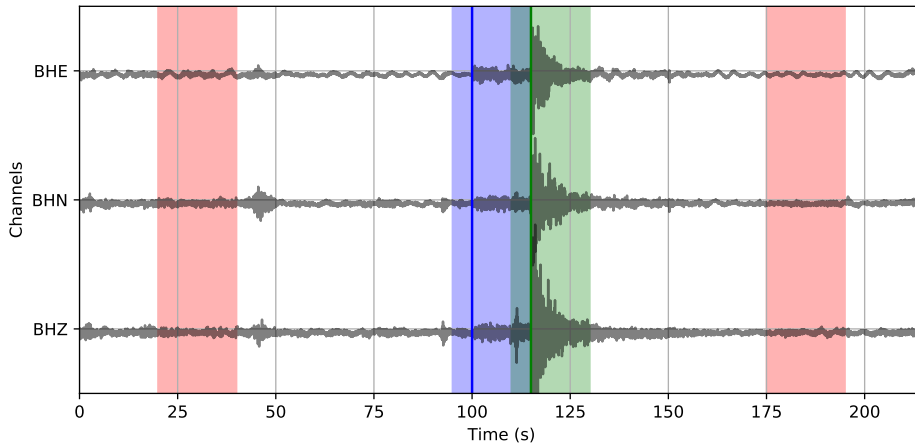


Figure A.1: An example of three-component seismogram recorded at station HSH from which 20-sec long time windows are extracted for both P (blue) and S (green) phases. Noise (red) windows are cut one-minute before P and after S phases. Sampling rate is 100 Hz. The arrival times of P and S phases are marked by vertical blue and green solid lines, respectively.

Appendix B. Pre-processing

Minimal preprocessing steps are performed on the raw seismic waveform in order to explore the limitations of “expressiveness” of the CNN. It is believed that a sufficiently complex CNN can take the necessary data manipulation, such as band-pass filtering, into account if it is learned to be significant to the final classification task.

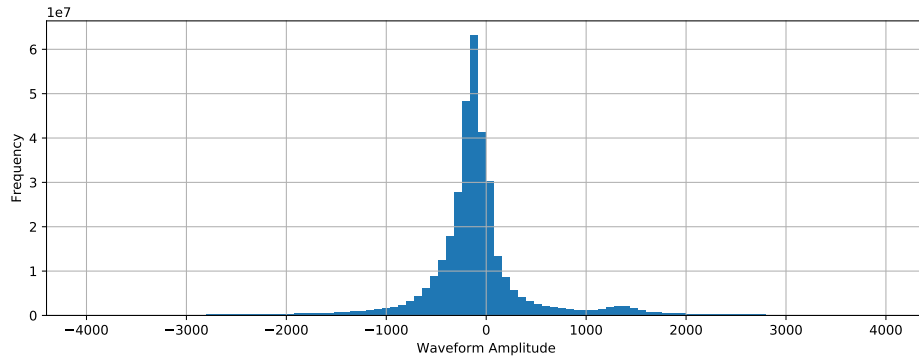
Soft-clipping method. On the other hand, we observed that the dynamic ranges of the labeled events vary dramatically from each other. This may result in the masking of weak events by stronger ones due to their amplitude difference. Moreover, higher precision may be required after batch normalization due to such differences. Since the GPU we used in this study works more efficiently for single-precision floating-point numbers, the dynamic range also imposes a hardware challenge. Hence, we apply a soft clipping process based on a logistic function, which is shown in Figure B.2b,

$$f(x) = 1/(1 + e^{-kx}) \tag{B.1}$$

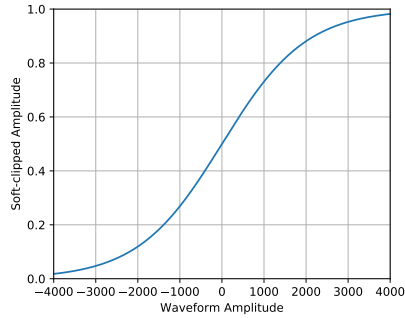
where x is the original amplitude, and k is chosen empirically based on the maximum amplitude in the original signal.

The soft clipping process, which is applied to all labeled data and continuous data with the same k value, keeps the input data range between 0 and 1, as well as reducing the relative amplitudes of strong and weak events. Figure B.2c illustrates that the soft-clipping process only suppresses the large amplitude signal while keeping the small one unchanged. Figure B.2a shows that the amplitude of most traces is less than 4000, thus we chose $k = 0.001$ and the resulting soft-clipping function is shown in Figure B.2b.

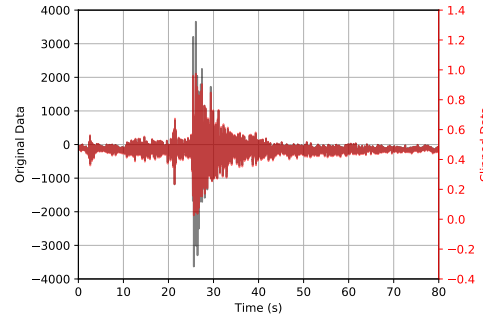
Effect of soft-clipping. During the CNN training process, the network is tested after every epoch to evaluate its accuracy. Figure B.3 shows the training loss, defined in equation (2), and testing accuracy, defined in equation (3), versus the number of epochs. The proposed network with soft clipping (red) reaches



(a) Distribution of waveform amplitude.



(b) Logistic Function with $k = 0.001$.



(c) Soft clipping effect

Figure B.2: Preprocessing for CPIC: (a) waveform amplitude distribution; (b) soft clipping with a logistic function on the input data and (c) example of soft-clipped signal. Note that large amplitude signals in the original input (black) are reduced significantly on the clipped signal (red) while the small amplitude part is unchanged.

97% accuracy after 40 epochs and becomes stable even though the training loss keeps going down. On the other hand, without soft clipping (blue and green), the validation accuracy of the network slowly increases but exhibits a large oscillation centered around 80% and 85% accuracy, even though the training loss continues to decrease. Thus with proper preprocessing, the trained CNN can reliably determine if a given 20-sec time window contains a P wave, S wave, or noise phase, and assess the likelihood of that decision.

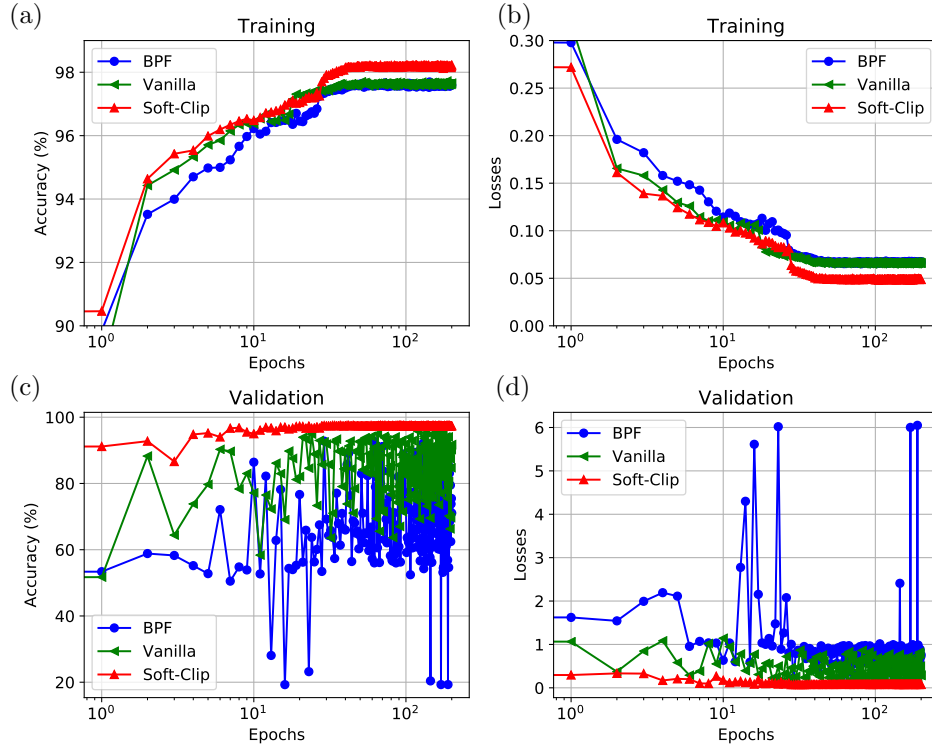


Figure B.3: Training process of 80%–20% chronological split with different preprocessing schemes: (a) Accuracy on Training Set, (b) Loss on Training Set, (c) Accuracy on Validation Set, (d) Loss on Validation Set. Soft-clip via logistic function in (c) is the most stable method and reaches highest validation accuracy.

Appendix C. Matched filter

The analysis procedure of matched filter detection generally follows Meng et al. (2013) and is briefly described here. Over 6,500 cataloged events between 2008/08/01 and 2008/08/30 are used to extract 6-sec templates. A 2–8 Hz band-pass filter is applied to enhance the strength of local earthquake signals, and the filtered waveforms are downsampled to 20 Hz. The 6-sec template window starts 1 s before either the P wave on the vertical component or the S wave on horizontal components. To avoid noisy traces, we measure the noise energy in a 6-sec window ahead of the template and define the corresponding signal-to-noise ratio (SNR) as the ratio between the energy of the template and noise energy.

Only traces with SNR above 5.0 are used to cross-correlate with continuous data and output the cross-correlation (CC) function. Stacked cross-correlation values on multiple stations are used to detect candidate events with a threshold of nine times the median absolute deviation (MAD) of the daily stacked correlation trace. We select 2008/08/30 as the testing day since it has the most cataloged events, approximately 300. Eventually, we end up with approximately 1,300 events and 12,200 phase picks that are detected on at least three stations.